

Quantifying Carbon Cycle Extremes and Attributing Their Causes Under Climate and Land Use & Land Cover Change from 1850 to 2300

Bharat Sharma^{1,2}, Jitendra Kumar³, Nathan Collier², and Auroop R. Ganguly¹, Forrest M. Hoffman^{2,4}

¹Sustainability and Data Sciences Laboratory, Department of Civil and Environmental Engineering, Northeastern University, Boston, Massachusetts, USA

²Computational Sciences & Engineering Division and the Climate Change Science Institute, Oak Ridge National Laboratory, Oak Ridge, Tennessee, USA

³Environmental Sciences Division, Oak Ridge National Laboratory, Oak Ridge, Tennessee, USA

⁴Department of Civil and Environmental Engineering, University of Tennessee, Knoxville, Tennessee, USA

Key Points:

- Human activities, through land-use change, lead to increased intensity, duration, and frequency of negative extremes in GPP.
- Soil moisture anomalies are the dominant driver of GPP extremes, followed by fire and daily maximum temperature.
- The regions with overall reduction in GPP often show weakening of negative extremes in GPP.

This manuscript has been authored by UT-Battelle, LLC, under contract DE-AC05-00OR22725 with the US Department of Energy (DOE). The US government retains and the publisher, by accepting the article for publication, acknowledges that the US government retains a nonexclusive, paid-up, irrevocable, worldwide license to publish or reproduce the published form of this manuscript, or allow others to do so, for US government purposes. DOE will provide public access to these results of federally sponsored research in accordance with the DOE Public Access Plan (<http://energy.gov/downloads/doe-public-access-plan>).

Corresponding author: Bharat Sharma, bharat.sharma.neu@gmail.com

This article has been accepted for publication and undergone full peer review but has not been through the copyediting, typesetting, pagination and proofreading process, which may lead to differences between this version and the Version of Record. Please cite this article as doi: [10.1029/2021JG006738](https://doi.org/10.1029/2021JG006738).

This article is protected by copyright. All rights reserved.

Abstract

The increasing atmospheric CO₂ mole fraction affects global climate through radiative (trapping longwave radiation) and physiological effects (reduction of plant transpiration). We use the simulations of the Community Earth System Model (CESM1-BGC) forced with Representative Concentration Pathway 8.5 to investigate climate-vegetation feedbacks from 1850 to the year 2300. Human-induced land use and land cover change (LULCC), through biogeochemical and biogeophysical processes, alter the climate and modify photosynthetic activity. The changing characteristics of extreme anomalies in photosynthesis, referred to as carbon cycle extremes, increase the uncertainty of terrestrial ecosystems to act as a net carbon sink. However, the role of LULCC in altering carbon cycle extremes under business-as-usual (continuously rising) CO₂ emissions is unknown. Here we show that LULCC magnifies the intensity, frequency, and extent of carbon cycle extremes, resulting in a net reduction in expected photosynthetic activity in the future. We found that large temporally contiguous negative carbon cycle extremes are due to a persistent decrease in soil moisture, which is triggered by declines in precipitation. With LULCC and global warming, vegetation exhibits increased vulnerability to hot and dry environmental conditions, increasing the frequency of fire events and resulting in considerable losses in photosynthetic activity. While most regions show strengthening of negative carbon cycle extremes, a few locations show a weakening effect driven by declining vegetation cover or benign climate conditions for photosynthesis. Increasing hot, dry, and fire-driven carbon cycle extremes are essential for improving carbon cycle modeling and estimation of ecosystem responses to LULCC and rising CO₂ mole fractions. Moreover, large aberrations in vegetation productivity represent potential and growing threats to human lives, wildlife, and food security.

Plain Language Summary

Rising carbon dioxide (CO₂) emissions due to human activities, such as fossil fuel burning and land use and land cover change (LULCC), are the major driver of climate change. Heatwaves, droughts, and fires have increased and are expected to accelerate with climate change in the twenty-first century and beyond. This increase in extreme climate conditions has the potential to further alter vegetation productivity (called gross primary production or GPP) and carbon uptake capacity. Here, we use a global Earth system model to investigate the impacts of (1) CO₂ forcing and (2) CO₂ and LULCC forcing

on the intensity, frequency, and duration of extreme events in GPP. We found that the negative extremes in GPP, which are associated with higher losses in carbon uptake than expected, increase at a higher rate than positive GPP extremes; and this rate rises with LULCC forcing. The most dominant climate driver causing the GPP extremes is soil moisture anomalies, which are triggered by extremes in precipitation and temperature. The lagged responses of climate drivers on GPP extremes vary with the drivers and spatial location. The largest number of GPP extremes were driven by the compound effect of water-, temperature-, and fire-related drivers.

1 Introduction

Human activities are altering the Earth's atmosphere, ocean, and land surfaces at a scale and magnitude not seen throughout the past multiple thousands of years. The rising concentration of greenhouse gases (GHGs) such as water vapor, ozone, carbon dioxide, methane, and nitrous oxide are primary drivers of global warming and climate change. As a result of continued growth in the global population, the demand for fossil fuels, crops, and wood is increasing. Enhanced emissions through use of fossil fuels (Le Quéré et al., 2018) and land use and land cover change (LULCC) increases the atmospheric concentration of carbon dioxide (CO_2). Rising CO_2 emissions have led to increased climate variability and frequency of climate extremes, which have a large impact on terrestrial gross primary productivity (GPP) and GPP extremes (Marcolla et al., 2020; Xian et al., 2020; Reichstein et al., 2013; Frank et al., 2015; Ichii et al., 2005; Piao et al., 2020). While climate extremes are relatively easy to measure, their impact on terrestrial vegetation is less detectable (Zscheischler et al., 2014). Since terrestrial ecosystems absorb a quarter of anthropogenic CO_2 emissions (Le Quéré et al., 2018), large changes in vegetation productivity could alter the global carbon budget. Hence, it is crucial to investigate extreme anomalies in terrestrial carbon cycle and estimate their impacts on the terrestrial carbon sink under rising CO_2 emissions and LULCC scenarios.

Prior studies (Zhu et al., 2016; Reichstein et al., 2013; G. Bonan, 2015) have found that the combined effect of CO_2 fertilization, increasing temperature, nitrogen deposition, and lengthening of growing seasons lead to increased vegetation productivity and strengthening of carbon sinks with a negative feedback to climate change. However, coupled carbon-climate models have large uncertainties in future projections of ecosystem responses and feedback strength (Hoffman et al., 2014; Reichstein et al., 2013; Frank et

al., 2015; Ichii et al., 2005). Hoffman et al. (2014) found persistent atmospheric CO₂ biases in Coupled Model Intercomparison Project 5 (CMIP5) models because of uncertainties in biological and physical processes related to carbon accumulation. While most Earth system model-based climate change studies analyze projections till year 2100, these projections may miss physical-biogeochemical feedbacks that arise later from the cumulative effects of climate warming (Moore et al., 2018). The negative sensitivity of terrestrial carbon cycle to rising temperature will likely have increasing adverse implications on carbon cycle extremes over time (Hubau et al., 2020; Frank et al., 2015). Understanding the direction and strength of these feedbacks is essential for estimating long-term CO₂ concentrations and predicting and mitigating the impact and extent of climate change. These limitations could alter the assessment of the rate of increase of atmospheric CO₂ and intensity of associated feedbacks with the terrestrial biosphere.

While the effects of increased warming due to greenhouse gases are spatially extensive, the LULCC effects are more regional (Pitman et al., 2012). The land-use history reconstruction used in this study estimated the proportion of land surface impacted by human activities to be 60% of total vegetated area, mainly due to conversions from primary vegetation to managed vegetation by 2100 (Hurt et al., 2011). The conversion of land from natural to managed ecosystems reduces the carbon sink and its capacity to uptake anthropogenic CO₂ and influences climate by modifying biogeophysical and biogeochemical processes (G. B. Bonan, DeFries, et al., 2012). Changes in the plant functional type (PFT) at any grid cell modifies the distribution of above and below ground carbon (Oleson et al., 2010), response to light and energy (G. B. Bonan et al., 2011), distribution of soil organic matter and nutrients (Koven et al., 2013). Human activities, such as the conversion of forests and grasslands to agricultural land and urbanization, alter net radiation, sensible and latent heat partitioning, biogeochemical cycles, and the hydrologic cycle. Reduction of temperate vegetation cover by deforestation increases the albedo of the surface which decreases the net radiation that drives surface cooling and reduces evapotranspiration that may result in declines in precipitation; but tropical deforestation for pastures decreases the total atmospheric column heating and atmospheric vertical motion which leads to a warmer and drier climate (G. B. Bonan, DeFries, et al., 2012; G. Bonan, 2015). Since interannual variability (IAV) in GPP is strongly influenced by interannual variations in radiation, temperature, and precipitation (Ichii et al., 2005),

116 the impact of LULCC in addition to CO₂ on carbon cycle extremes will likely increase
117 over time.

118 Recent studies have investigated the characteristics of extreme anomalies in GPP
119 due to climate change until the year 2100 (Zscheischler et al., 2014; Frank et al., 2015;
120 Flach et al., 2020; Reichstein et al., 2013) and a few concluded that losses in carbon up-
121 take due to negative extremes in GPP are compensated by increased CO₂ fertilization
122 (Zscheischler et al., 2014; Reichstein et al., 2013). However, to our knowledge, no study
123 has examined the extreme anomalies in carbon cycle beyond 2100 and the role of human
124 LULCC in modifying carbon cycle extremes.

125 Rising CO₂ and LULCC impact many components of the terrestrial carbon cycle,
126 such as total ecosystem carbon, net biome productivity, net ecosystem productivity, net
127 primary productivity, and GPP. The overarching goal of this study is to investigate the
128 role of CO₂ and LULCC in modifying the characteristics of extremes in GPP, referred
129 to as carbon cycle extremes in this paper, and attribute changes to individual and com-
130 pound effects of climate drivers. We hypothesize that 1) rising CO₂ emissions will lead
131 to larger increases in the intensity, frequency and duration of negative carbon cycle ex-
132 tremes than positive extremes; and 2) LULCC activities in addition to CO₂ emissions
133 will further increase GPP interannual variability and magnitude of carbon cycle extremes
134 though total GPP will reduce. We performed analysis to 1) examine the magnitude, du-
135 ration, frequency and spatial distribution of negative and positive carbon cycle extremes;
136 2) investigate the lagged response of antecedent climate drivers (and their compound ef-
137 fect) that drive carbon cycle extremes; 3) analyze the climate conditions that trigger long
138 duration temporally continuous extremes; and 4) inspect regional changes in climate-carbon
139 feedbacks for the Central and South American tropics.

140 2 Data

141 We used simulations of the Community Earth System Model (version 1) with bio-
142 geochemistry enabled, CESM1(BGC), at approximately 1° × 1° resolution to analyze
143 climate-driven extreme anomalies in total photosynthetic activity. CESM1(BGC) is a
144 fully coupled global climate model composed of land, atmosphere, and ocean components
145 (Lindsay et al., 2014; P. J. Lawrence et al., 2012). The atmospheric CO₂ forcing time
146 series consisted of the historical (1850–2005), Representative Concentration Pathway 8.5

(RCP 8.5; 2006–2100), and Extended Concentration Pathway (ECP 8.5; 2101–2300) mole fractions, which increased from 285 ppm in 1850 to 1962 ppm in 2300 (Figure 1(a)). Analysis of the Coupled Model Intercomparison Project 5 (CMIP5) models using the International Land Model Benchmarking (ILAMB) (Collier et al., 2018) show (Table S1) that CESM1(BGC) is one of the best performing model in terms of overall and IAV benchmark scores when compared to observational benchmarks.

We analyzed terrestrial carbon cycle extremes (or GPP extremes) using two simulations, namely, *with* and *without LULCC*. In the simulation *without LULCC*, the land cover was fixed at pre-industrial (year 1850) values. In the *with LULCC* simulation, transient land cover was prescribed over the historical and RCP 8.5 period (1850–2100) (Hurt et al. (2011)) and consists of the prescribed spatial distribution of PFTs (P. J. Lawrence et al. (2012)). Land-use conversion is assumed to stop at the year 2100, and the distribution of PFTs remains constant at year 2100 level for the period 2100 – 2300, while wood harvest is maintained at a constant rate over that period (Mahowald et al., 2017). The reactive nitrogen deposition followed the spatially variable time series from 1850 to 2100 (Lamarque et al., 2010) and was subsequently held constant from 2100 to 2300. Biogeochemical processes on land and in the ocean respond to the historical and prescribed RCP 8.5 and ECP 8.5 atmospheric CO₂ concentration forcing (Figure 1(a)). Increasing CO₂ fertilization, water-use efficiency, and lengthening of growing seasons enhance total photosynthesis and gross primary production (GPP). These processes will be further altered by the changes in PFT distribution under *with LULCC*. Figure 1(c) shows the 5 year moving average of global annually integrated GPP for simulations *with* and *without LULCC*, both forced with the same atmospheric CO₂ concentration trajectory (Figure 1(a)). The magnitude of the average GPP *with LULCC* is less than the average GPP *without LULCC* potentially due to the conversion of primary vegetation to managed vegetation.

3 Methods

A significant deviation from the mean value is called an extreme. Extreme events in GPP signify large variations in photosynthetic activity, with positive extremes representing increases in carbon uptake, while negative extremes being indicative of loss of carbon uptake (Zscheischler et al., 2014). While extremes in climate have been extensively studied (Reichstein et al., 2013; Seneviratne & Hauser, 2020; Ban et al., 2015; Frank et al., 2015; Flach et al., 2020), few studies have focused on extremes in GPP and their

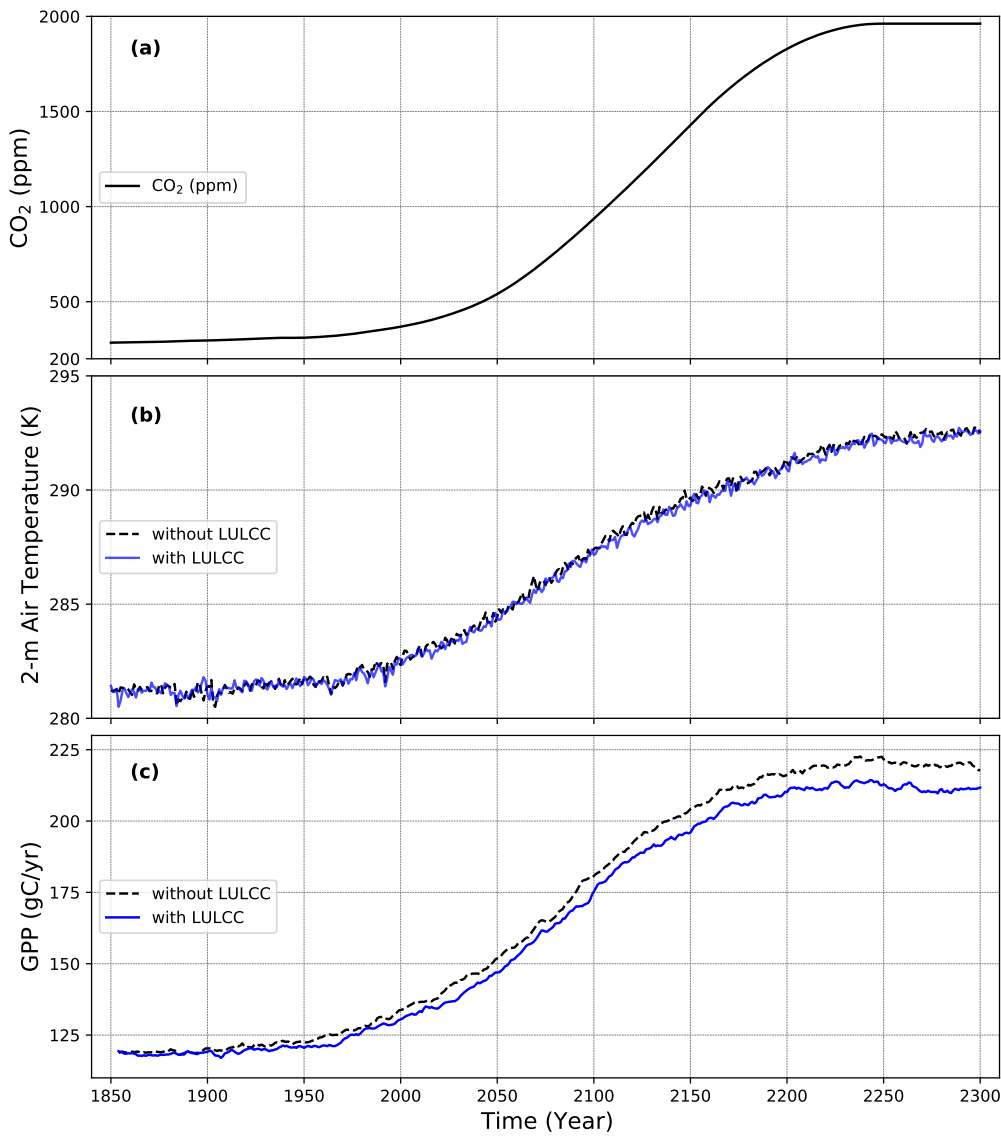


Figure 1: The (a) prescribed trajectory for atmospheric carbon dioxide (CO₂) forcing, (b) 5-year running mean of annual 2 m air temperature, and (c) 5-year running mean of total annual gross primary production (GPP) for the historical, RCP 8.5 and ECP 8.5 simulations.

underlying drivers(Zscheischler et al., 2014; Xu et al., 2019; Flach et al., 2020). In this study, we identify extremes in global carbon uptake by computing percentile-based thresholds (Seneviratne et al., 2012). Described in detail in Section 3.1, a positive (or negative) extreme in GPP is defined as anomalies in GPP that are greater (or less) than a selected percentile-based threshold of GPP anomalies. The thresholds were computed by selecting 1st and 99th percentile anomalies in GPP, calculated at every land grid cell for each consecutive 25 years from the year 1850 through 2300. The GPP extreme events are then defined as values of GPP anomalies above q (positive extremes) or below $-q$ (negative extremes). The schematic Figure 2 illustrates the steps to compute GPP extremes.

Extremes in GPP could also be categorized as isolated vs temporally continuous extreme events. The isolated and temporally continuous extremes in GPP are analogous to hot days and heatwaves. Extreme events in GPP that are continuous in time represent a significant cumulative impact on carbon uptake. Akin to the definition of temporally continuous heatwaves by Baldwin et al. (2019), we define a temporally continuous extreme (TCE) event (Figure S1) in GPP as (a) three or longer months (equal to a season length) of GPP extreme anomaly occurring consecutively, (b) and are considered as single continuous event through any gaps of two months or shorter in duration (assuming that ecological recovery is unlikely in less than a season) beyond three months. A GPP TCE event that occur after a season, i.e., three months or more, is considered a separated TCE. Section 3.2 illustrates the method for attribution of GPP TCEs to individual and compound effects of climate drivers.

3.1 Identification and Detection of GPP Extreme Events

The time series of GPP at any grid cell consists of a trend, seasonality, and anomalies (Figure 2) components. We used singular spectrum analysis (SSA), a non-parametric spectral estimation method based on embedding a time series in vector space (Golyandina et al., 2001), to extract signals with specific frequencies. The trend in GPP at any grid cell captures long term change in mean GPP, which is influenced by long term changes in climate drivers, atmospheric CO₂ concentration, and LULCC. Since El Niño-Southern Oscillation (ENSO), and to a lesser extent other large-scale drivers of climate variability, enhance the variability in terrestrial photosynthesis, the nonlinear trend at each grid cell was calculated by adding all the frequencies of 10 years and longer. Hence, carbon

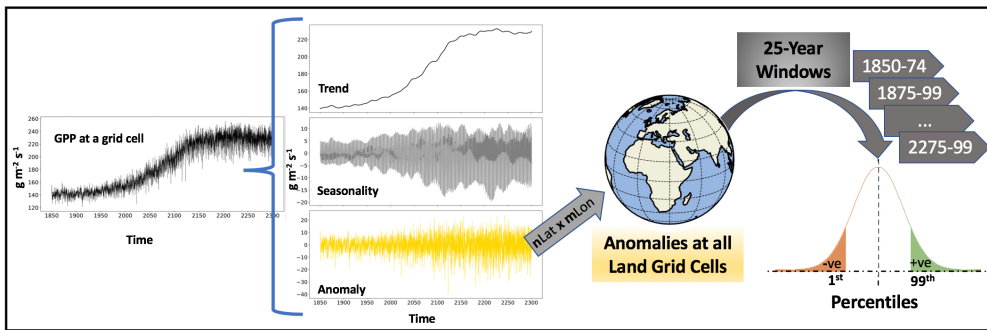


Figure 2: Schematic diagram for calculating thresholds in gross primary production (GPP). The anomalies are calculated at every grid cell by subtracting the nonlinear trend and modulated annual cycle from the GPP time series. The anomalies of every land grid cell ($nLat \times nLon$) for consecutive 25 year time windows were chosen to calculate probability distribution function of GPP anomalies. The 1st and 99th percentile values represent the global GPP threshold values for negative and positive extremes in GPP.

cycle extremes in our study include the GPP anomalies induced by ENSO which is one of the largest modes of climate variability and peaks about every three to seven years (Chylek et al., 2018) and exerts strong regional effects on the terrestrial carbon cycle (Poveda et al., 2001). The seasonality in GPP follows a periodic cycle of 12 months. The conventional way to compute the annual cycle is to determine the mean climatology over a period, however, the climatology does not reflect the intrinsic nonlinearity of the climate-carbon feedback, especially under external forcing (Wu et al., 2008) because of the increased modulation of the annual cycle in GPP under business-as-usual rising CO₂ emissions. We calculated the modulated annual cycle, which allows the annual cycle to change from year to year and consists of signals with a frequency of 12 months and its harmonics. The anomalies at each grid cell were calculated by subtracting the trend and modulated annual cycle from the GPP time series (Figure 2). Hence, GPP anomalies comprised of the high-frequency signals (<12 months) and the interannual variability (>12 months and <10 years). We examined the probability distribution function (PDF) of GPP anomalies for all land grid cells for every 25-year time window from 1850 through 2300. While the left tail of the PDF of GPP anomalies represents large losses in carbon uptake, the right tail portrays large gains in carbon uptake. We chose the 1st and 99th percentile of

228 all GPP anomalies as thresholds in the 25-year time windows to identify large losses and
 229 gains in carbon uptake.

230 The percentile-based thresholds (1st and 99th) for every 25-year time window yield
 231 the negative ($Th-$) and positive ($Th+$) threshold trajectories of GPP anomalies. The
 232 extreme anomalies in GPP range from 425 GgC/month for the period 1850–74 to 840 GgC/month
 233 for 2275–99, as shown in Figure 3. Since GPP anomalies are a subset of GPP, increasing
 234 CO₂ fertilization, water use efficiency, and lengthening of growing season lead to in-
 235 creases in GPP (Figure 1(c)) and the thresholds of GPP anomalies. The simulations *with*
 236 and *without LULCC*, show higher magnitudes of $Th-$ than $Th+$, indicating that neg-
 237 ative anomalies in GPP are stronger than positive for the same percentile. Also, the val-
 238 ues of the thresholds for simulation *with LULCC* were higher than *without LULCC*. To
 239 enable the comparison of simulations *with* and *without LULCC*, we selected one thresh-
 240 old trajectory, *without LULCC TH+ (q)*, to apply for calculations of all positive and
 241 negative extremes in the current study. Thus, the positive GPP extremes are defined as
 242 GPP anomalies greater than q and negative GPP extremes are the GPP anomalies less
 243 than $-q$ for both simulations, *with* and *without LULCC*.

244 Integral of negative (or positive) GPP extremes over land grid cells represents the
 245 total global loss (or gain) in carbon uptake per month. The time series of frequency and
 246 extent (area) under GPP extremes was computed by integrating the count and area of
 247 grid cells under GPP extremes.

248 3.2 Attribution to Climate Drivers

249 Human activities, through fossil fuel emissions and land cover changes, modify the
 250 climate and climate-carbon feedbacks. To attribute significant changes in carbon uptake
 251 and GPP to climate drivers, we computed linear regression of temporally continuous GPP
 252 extremes with anomalies in atmospheric precipitation (*Prcp*, composed of atmospheric
 253 rain and snow), precipitation minus evapotranspiration (*P-ET*), soil moisture (*Soilmoist*,
 254 up to 1-m depth), monthly maximum daily temperature (*T_{max}*), monthly minimum daily
 255 temperature (*T_{min}*), monthly mean daily temperature (*T_{sa}*), and fire (*Fire*, total column
 256 level carbon loss due to fire) (Table 1).

257 The impact of climate drivers on GPP often has a lagged response because the ter-
 258 restrial ecosystem has ingrained plasticity to buffer and push back effects of climate change

Table 1: Climate Drivers Considered for Attribution to GPP Extremes

Symbol	Units	Description
P_{rcp}	mm s^{-1}	Atmospheric rain + snow
$P-ET$	mm s^{-1}	Precipitation minus Evapotranspiration
$Soilmoist$	mm	Soil moisture in top 1-m depth
T_{\max}	K	Monthly maximum daily temperature
T_{sa}	K	Monthly mean daily temperature
T_{\min}	K	Monthly minimum daily temperature
$Fire$	$\text{gC m}^{-2} \text{ s}^{-1}$	Total column level carbon loss due to fire

(Zhang et al., 2014). The controls of different climate drivers on GPP and its extremes is also dependent on location, timing, soil type and moisture, and vulnerability of land cover type (Frank et al., 2015). Therefore, at every location of GPP TCEs, we used linear regression to compute the correlation of TCEs with the cumulative lagged response of anomalies of every climate driver at time-lags of 0 to 12 months, for every 25 year time window from 1850 to 2300. However, lagged responses beyond four months were insignificant and thus we only report on one, two, and three lags. Anomalies from past months were included in the computation of lagged correlations. For instance, to compute a climate-carbon lag response of 3 months, the GPP extreme anomalies at month t were correlated with the average of climate driver anomalies at $t-3$, $t-2$, and $t-1$ months. We also investigated the GPP TCEs driven by triggers (climate drivers during onset of TCEs) and persistent climate drivers (considering entire duration of TCEs). We identified the most dominant climate driver at any grid cell under simulations *with* and *without LULCC*, as the climate driver with the highest absolute correlation coefficient (significance value, $p < 0.05$). The percent global distributions of dominant drivers for every time window were computed to inspect the changing patterns of dominant drivers at various lags and over time.

A GPP TCE event could be driven by one or a combination of climate drivers. The study of compound events consisting of multiple different climate drivers leading to a GPP extreme improves our understanding of interactive effects of climate drivers (Zscheis-

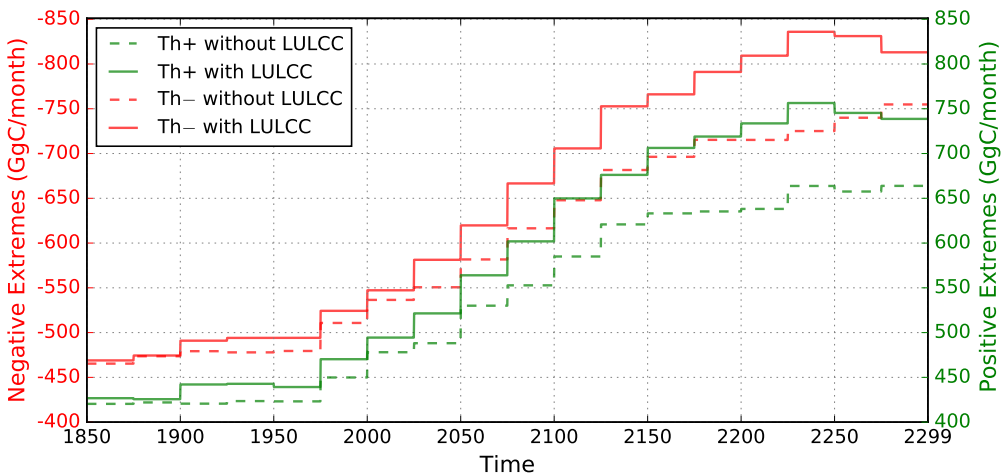


Figure 3: Thresholds of GPP extreme events with and without LULCC from 1850–2299.

The figure shows increasing thresholds of positive and negative GPP extreme events based on 99th and 1st percentile. The percentiles are calculated for global GPP anomalies for every time window (of 25 years) from 1850–2299. The red color represents negative thresholds or $Th-$ and green represents $Th+$. The solid and dashed lines represent the simulations with and without LULCC respectively.

chler et al., 2018). While the climate extremes and carbon extremes often do not occur concurrently, the compound effects of climate drivers that are not climate extremes can nevertheless impact the carbon cycle (Pan et al., 2019). We studied the compound effects of water ($Precip$, $P-ET$, and $Soilmoist$)-, temperature (T_{max} , T_{sa} , and T_{min})- and fire ($Fire$)-driven TCEs in GPP.

4 Results

4.1 Detection and Identification of GPP Extremes

The 1st and 99th percentiles of the PDF of GPP anomalies for all land grid cells in 25-year time windows were used to compute the threshold trajectories for *with* and *without LULCC* simulations. Figure 3 shows trajectories of positive and negative GPP extremes for simulations *with* and *without LULCC*. The rising atmospheric CO₂ concentrations and increasing CO₂ fertilization, water use efficiency and lengthening of growing seasons (G. Bonan, 2015; P. J. Lawrence et al., 2012) lead to an increase in the global GPP and GPP anomalies. Consequently, $Th+$ and $Th-$ increased in both simulations;

for the simulation *without LULCC* $Th+$ increased from 420 GgC/month during 1850–1874 to 664 GgC/month during 2275–2299; the corresponding values for $Th+$ *with LULCC* were 426 and 739 GgC/month, for $Th-$ *without LULCC* were –465 and –755 GgC/month, and for $Th-$ *with LULCC* were –469 and –813 GgC/month. The increasing magnitude of thresholds for GPP extremes over time highlights the intensification of GPP extremes over time. For the same percentile, the magnitude of negative thresholds were larger compared to positive thresholds. Hence, negative anomalies in GPP or losses in carbon uptake were much larger than gains in carbon uptake, primarily due to negative impact of increasing anthropogenic CO₂ and LULCC on carbon cycle anomalies. Higher thresholds for the simulation *with LULCC* despite lower GPP (Figure 1(c)) compared to the simulation *without LULCC*, highlights that increasing magnitude of GPP anomalies were likely due to LULCC and wood harvest. Higher anomalies GPP is potentially due to large reductions in the area of tree PFTs of primary vegetation (forests) in the RCP 8.5 LULCC scenario, -3.5×10^6 km² from 1850 to 2100. The decrease in primary vegetation is associated with large increases in crop and grass areas, leading to a reduction of ecosystem carbon of –49 PgC from 1850 to 2100. The global wood harvest carbon flux increased to 4.2 PgC year^{–1} (P. J. Lawrence et al., 2012) in the year 2100, and then was kept at a constant harvest rate from 2100 to 2300. The legacy effects of human land cover change and continued wood harvest becomes more visible beyond 2100 when the difference in annual GPP of both simulations widens (Figure 1(c)). As a result of enhanced variability in GPP *with LULCC*, we saw a larger magnitude of negative and positive thresholds for the simulation *with LULCC* (Figure 3).

The global time series of the intensity of losses and gains in carbon uptake, calculated by integrating negative and positive extremes in GPP, are shown in Figures 4(a) and 4(b) for simulations *without* and *with LULCC*, respectively. Compared to the simulation *without LULCC*, the total additional loss of global carbon uptake due to LULCC was –46.53 PgC for period 1850–2100 and –141.76 PgC for 2101–2300. The respective difference in total global GPP (*with LULCC* minus *without LULCC*) was –676 PgC for 1850–2100 and –1416 PgC for 2101–2300; and relative to the total global GPP, the additional losses in total carbon uptake due to LULCC increased from 6.9% (1850–2100) to 10% (2100–2300). Hence, LULCC impacts global carbon cycle by reducing the total global GPP and increasing losses in carbon uptake during GPP extremes. The rates of increase in the intensity of positive extremes in GPP for the simulation *without LULCC*

Accepted Article

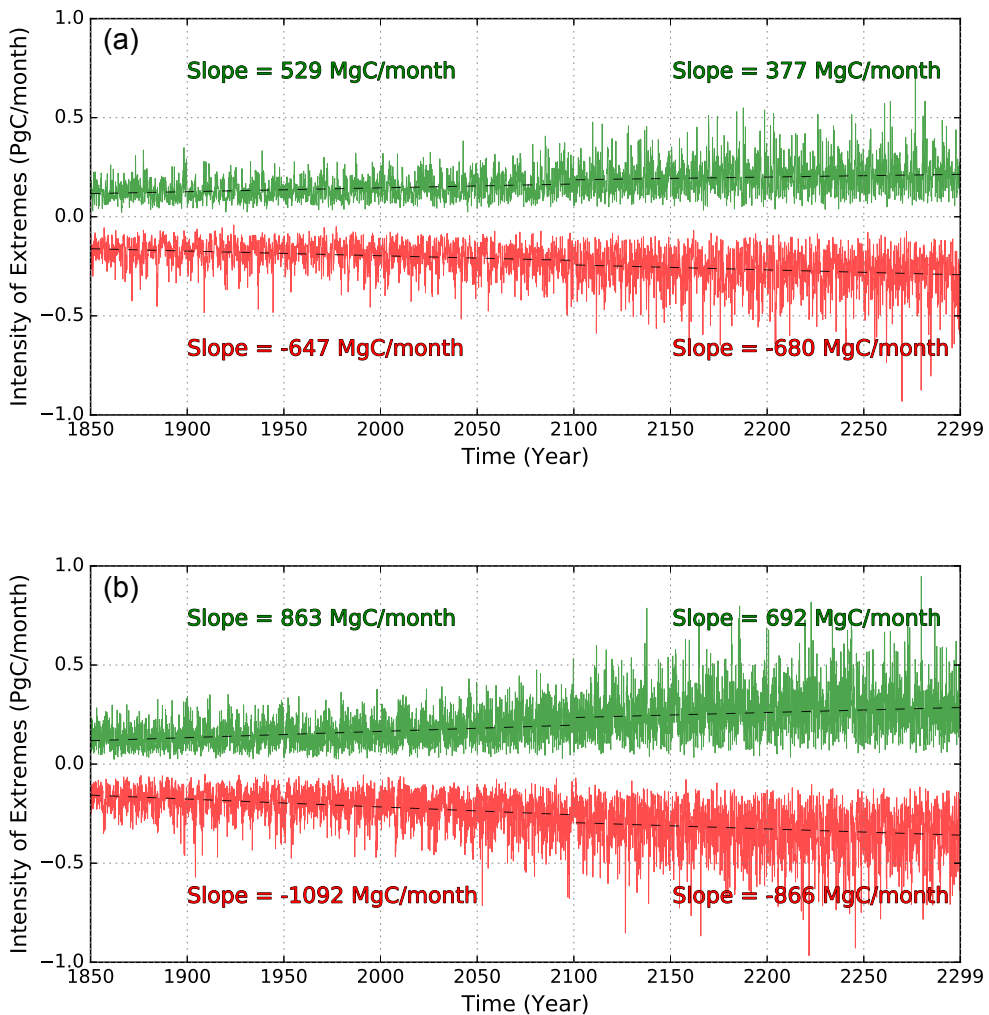


Figure 4: Monthly time series of intensity of global GPP extreme events for the simulation without LULCC (a) and with LULCC (b) from 1850–2299. The positive GPP extremes, GPP anomalies $> q$, are represented in green color and the negative extremes, GPP anomalies $< -q$, are shown in red color. The rate of increase of positive GPP extremes without LULCC are 529 MgC/month from 1850–2099 and 377 MgC/month from 2100–2299 (a). The corresponding rates for the growth of negative extremes are -647 MgC/month and -680 MgC (a). The rate of increase of positive GPP extremes with LULCC are 863 MgC/month from 1850–2099 and 692 MgC/month from 2100–2299 (b). The corresponding rates for the growth of negative extremes are -1092 MgC/month and -866 MgC (b).

were 529 and 377 MgC/month for the periods 1850–2100 and 2101–2299, respectively, and for the simulation *with LULCC* were 863 and 692 MgC/month, respectively. The corresponding rates of increase in the intensity of negative extremes in GPP for the simulation *without LULCC* were –647 and –680 MgC/month, respectively, and for the simulation *with LULCC* were –1092 and –866 MgC/month, respectively. The changes in the rates of the intensity of positive extremes in GPP for the simulation *with LULCC* were analogous to the simulation *without LULCC*. However, the intensity of negative extremes in GPP for the simulation *with LULCC* shows a decrease beyond 2100, possibly due to non-increment of wood harvest rate and a constant PFT distribution at the year 2100 values for the period from 2100 through 2300 which decreases the relative variability in GPP after 2100. The larger intensity of negative extremes in GPP for the simulation *with LULCC* than *without LULCC* could result from increased wood harvest and land conversions to agriculture, pastures, and urban areas. The rate of increase in the intensity of positive extremes in GPP was higher in the simulation *with LULCC* than *without LULCC* probably due to large re-growth of secondary forests in the regions of the Eastern U.S., Europe, Africa, and South America (Hurtt et al., 2011). In the simulation *with LULCC*, by the year 2100 under RCP 8.5, the LULCC transitions resulted in high-density croplands in the U.S., Europe, and South East Asia; high-density pastures in the Western U.S., Eurasia, South Africa, and Australia (Hurtt et al., 2011). Primary forests were present in high northern latitudes and parts of Amazonia. Hence, LULCC forcing coupled with CO₂ forcing under RCP 8.5 and ECP 8.5 intensified both losses and gains in carbon uptake during extremes in GPP, with net losses in carbon uptake dominating the net climate-carbon response.

The rate of increase of intensities of positive and negative extremes in GPP was stronger for the simulation *with LULCC*, although the total GPP was less than the simulation *without LULCC* (Figure 1(c)). Stronger intensities of GPP extremes *with LULCC* were due to the larger interannual variability (IAV) in GPP *with LULCC* compared to *without LULCC* (Figure 5). LULCC alters the climate by modifying the biogeochemical and biogeophysical processes, which further affects the carbon cycle. For example, in semiarid climates, loss of vegetation cover increases the surface albedo, which increases the reflected solar radiation and cools the surface climate that weakens the boundary layer, reducing the probability of precipitation that creates the dry climate and reduces plant productivity. Biogeochemical processes include uptake of carbon during photosynthe-

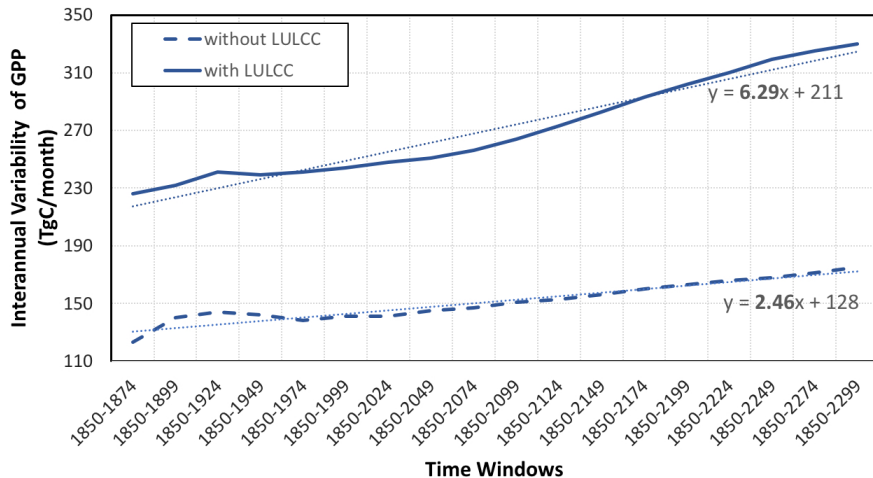


Figure 5: Global interannual variability (IAV) of GPP with and without LULCC. The unit of IAV is 10^{12} gC. The IAV is calculated from 1850 as the base year to 25 year increments, as shown on the *x*-axis. The solid line represents the IAV of GPP with LULCC and dashed line represents the IAV without LULCC. The linear fits represented by dotted lines show rates of increase of IAV of GPP with LULCC, which is higher by a factor of 2.5 compared to the simulation without LULCC.

sis at an increased atmospheric concentration of CO₂ and loss of carbon during respiration in a warmer climate. Biogeophysical and biogeochemical processes do not occur in isolation and depend on the hydrologic cycle (G. Bonan, 2015). With increases in atmospheric CO₂ concentration, the climate becomes warmer and increases the intensity of precipitation and accompanying precipitation extremes (Ban et al., 2015; O’Gorman, 2015). Clearing of land and deforestation has led to and will lead to cooling in high latitudes, warming in tropics, and uncertain changes in mid-latitudes (D. M. Lawrence et al., 2016). As a result, human LULCC increases the regional heterogeneity in vegetation that alters the climate drivers (Ichii et al., 2005), further increasing the global interannual variability and anomalies of GPP as well as the spatially heterogeneous distribution of GPP extremes. Therefore, the effect of both CO₂ and LULCC forcing, represented in *with LULCC*, increases the variability of biogeochemical and biogeophysical feedbacks, thus resulting in increased IAV of GPP in *with LULCC* than *without LULCC*.

The regional atmospheric circulation and climate change lead to spatial variations in the distribution of GPP extremes and the intensities of GPP extremes. Since the def-

374 initiation of GPP extremes is based on the threshold trajectory of 1st percentile global anomalies
375 of GPP for consecutive 25-year time windows in the simulation *without LULCC* (Figure 3), the total number of grid cells under positive GPP extremes were constant at around
376 64,000 (for every 25-year time windows) while they vary for all other scenarios. The total
377 number of grid cells and area affected by negative extremes in GPP for the simulation
378 *with LULCC* were largest, possibly because of increased negative feedback of climate
379 variability on the carbon cycle due to the cumulative CO₂ and LULCC forcing. Relative
380 to the frequency of positive extremes in GPP for the year 1850 (*without LULCC*), the frequency
381 of positive extremes (*with LULCC*) increased by 17% and 28% for the periods 1850–2100 and
382 2101–2300 respectively; and the respective growth rates of negative extremes
383 (*with LULCC*) were 13% and 19%. For *with LULCC*, growth rates for the area affected by
384 positive GPP extremes were 16% and 28%, and for negative GPP extremes at 12% and 20% during
385 1850–2100 and 2101–2300 respectively. Higher growth rates of frequency and area-affected by
386 positive extremes in GPP were probably due to increases in secondary forest cover; however the losses in the expected carbon uptake due
387 to LULCC were larger than gains.

389 4.2 Attribution to Climate Drivers

390 The attribution of climate-driven extremes in GPP were performed for GPP TCE events,
391 which are time-continuous GPP extremes meeting the criteria described in section 3. Variability in terrestrial carbon cycle intensified the climate-driven GPP TCEs
392 under the combined forcing of human-induced LULCC and anthropogenic CO₂ emissions.
393 The mean duration (Figure 6(a)) and standard deviation (Figure S2) of negative and positive
394 TCEs in GPP for the simulation *with LULCC* were greater than the simulation *without LULCC*. In addition, the duration of TCEs lengthened over time, with more long-
395 duration TCEs and fewer short-duration TCEs as time progressed. Figure 6(b) shows
396 the density plot of the count of negative TCEs in GPP vs. the total duration of GPP
397 TCEs in 25-year windows for the simulation *with LULCC*. The increasing mean duration
398 of the negative TCEs in GPP in the future likely causes a larger reduction in the
399 carbon uptake, which has significant implications for carbon storage and the carbon budget,
400 and it can negate the positive feedback of increasing CO₂ fertilization under RCP 8.5
401 and ECP 8.5 CO₂ scenarios.

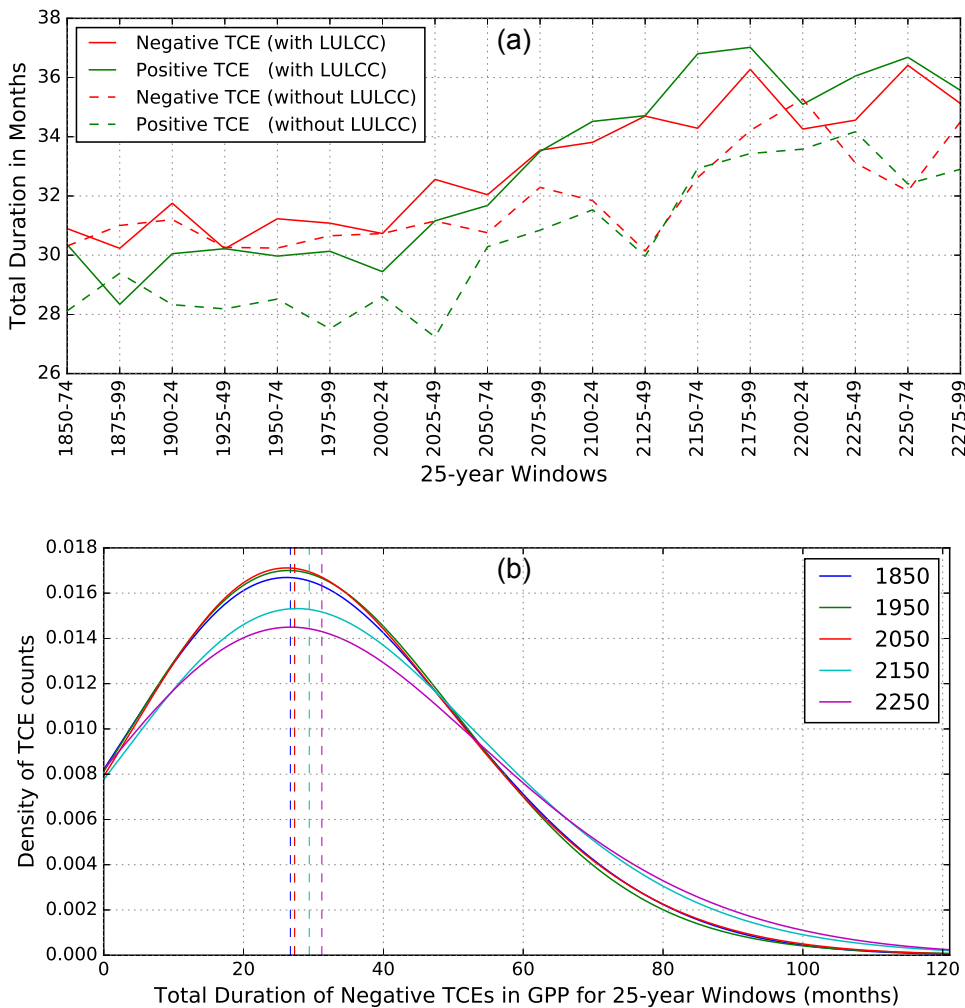


Figure 6: The mean duration of positive (shown in green) and negative (shown in red) TCEs for both the simulations, with (solid lines) and without (dashed lines) LULCC, for 25-year periods (a). The probability density of counts of total number of months under a negative TCEs in 25 years or 300 months (as shown in x -axis) for 25-year windows starting at the years 1850, 1950, 2050, 2150 and 2250 with LULCC (b). The dashed vertical lines shows the shifting of mean duration of negative TCEs to right, highlighting that the TCEs are getting longer over time.

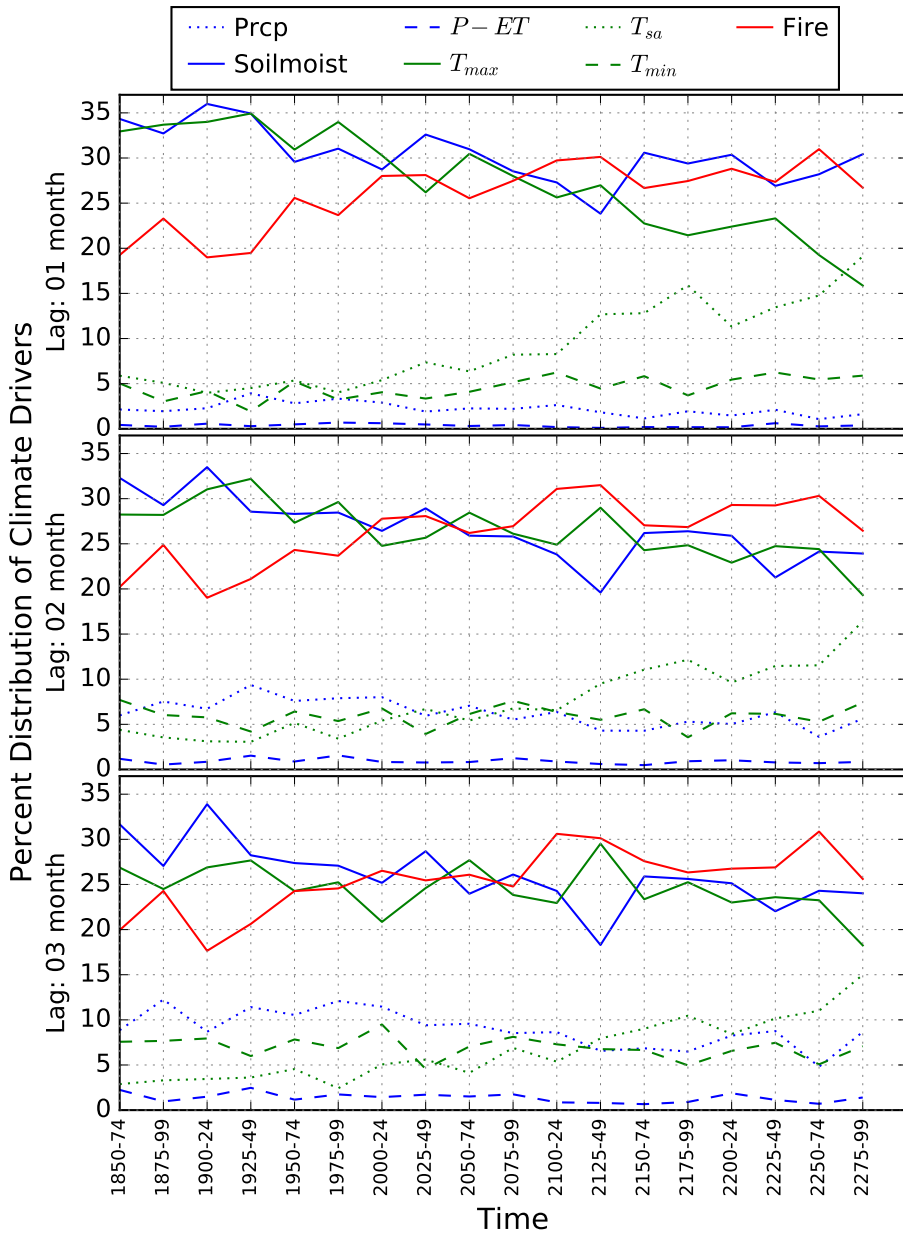


Figure 7: Percent distribution of global dominant climate drivers with LULCC for every time window from 1850–2299. For a particular lag month (1, 2, 3, etc.), a climate driver with highest correlation coefficient ($p < 0.05$) with carbon cycle TCEs at any grid cell is called a dominant climate driver.

Extremes in carbon cycle and climate extremes often do not occur simultaneously (Pan et al., 2019). In this study, we first detect temporally continuous extremes (TCEs) in GPP and then attribute the climate drivers using linear regression. Pearson's correlation coefficients and corresponding significance values (p -values) were computed between every climate driver and extreme anomalies in GPP during TCEs. The dominant climate driver at every land grid cell was defined by the maximum absolute correlation coefficient of climate drivers ($p < 0.05$). To consider the response of the ecosystem to prevailing climatic conditions, linear regressions were performed at multiple lags between extreme anomalies in GPP and climate driver anomalies. Figure 7 (and Figure S3) show the percent distribution of dominant climate drivers for every 25-year time window for both simulations, *with LULCC* and *without LULCC*, respectively, at lags of 1, 2, and 3 months. The relationship of water availability (soil moisture) with TCEs in GPP was globally dominant during most time windows (Figure 7). Reduction in soil moisture leads to an anomalous reduction in photosynthesis (Frank et al., 2015). Soil moisture is the most dominant driver of negative carbon cycle extremes, highlighting a strong positive correlation of plant productivity with soil moisture, as shown in Figure S4(b). Temperature (T_{\max} and T_{sa}) and *Fire* have a negative correlation with TCEs in GPP (spatial distribution shown in Figures S4(d) and S4(e)), where an anomalous increase in these drivers leads to loss in carbon uptake. T_{\max} was dominant at a lag of 2 months through 2100, but *Fire* shows dominance at higher lags, especially beyond 2100 in the simulation *without LULCC*. The percent count of dominant temperature drivers, T_{\max} and T_{sa} , increased over time, especially after 2100. Hence, carbon extremes driven by hot conditions will have the largest increase in a warming climate, especially after 2100. The lagged response of anomalously hot air temperatures and lack of soil moisture creates hot and dry conditions suitable for fire events. Fire events driven by hot and dry conditions increase at a higher rate at all lags in the simulation *with LULCC* than the simulation *without LULCC*. After 2100 in the simulation *with LULCC*, fire stands out as the dominant driver at all lags, highlighting that the human-induced LULCC will make ecosystems more vulnerable to fire events. The results of our study are consistent with the findings of Williams et al. (2014) and Zscheischler et al. (2014), suggesting that the declines in GPP with warm temperature extremes are due to dependence of GPP on soil moisture, and to the strong negative correlation between soil moisture and temperature. The rising temperature under global warming will create a warmer environment in the

438 future, increasing the risk associated with heatwaves and their impacts on the ecosys-
439 tem. A decline in precipitation and soil moisture compounded with warm temperature
440 may cause an unprecedented increase in loss of carbon uptake and potentially reduce the
441 terrestrial carbon sink.

442 The combined effect of climate drivers often has a larger impact on extremes in car-
443 bon cycle than the simple addition of individual climate drivers (Zscheischler et al., 2018, 2014;
444 Frank et al., 2015; Flach et al., 2020). To capture the compound effect of climate drivers
445 (Table 1) on GPP TCE events, the climate drivers were grouped under fire, tempera-
446 ture, and water-driven extremes (Section 3.2). Figures 8 and S5 show the spatial distri-
447 bution of climate drivers at a lag of one month for simulations *with* and *without LULCC*,
448 respectively. We observed an increase in the number of TCEs in GPP and changes in
449 the spatial distribution of GPP TCEs and climate drivers for time periods 1900–24, 2000–
450 24, 2100–24, and 2200–24 in the simulation *with LULCC* (Figure 8). Most locations ex-
451 perienced TCE events due to the combined effects of all the climate drivers.

452 We computed all combinations of water (dry or wet), temperature (hot or cold),
453 and fire-driven climatic conditions that cause GPP TCEs. For brevity, we report results
454 for one 25-year time window one per century. The fractions (larger than 0.05) of total
455 negative TCEs in GPP driven by mutually exclusive climate conditions are shown in Fig-
456 ure 9. More than half of the total TCEs in GPP occurred when the environmental con-
457 ditions are hot and dry, resulting in fire events and account for large reductions in GPP
458 (Figure 8 and 9). Similar to other studies (Zscheischler et al., 2014; Frank et al., 2015),
459 a stronger correlation between warm and dry climate has a substantial impact on the
460 terrestrial carbon cycle. The increased fraction of TCEs attributed to hot climate over
461 time is possibly due to combined attribution of T_{\max} and T_{sa} , as shown in Figure 7. Fig-
462 ure S6 represents the total fraction of TCEs in GPP driven by mutually inclusive climatic
463 conditions. As global warming increases the temperature of the planet, ecosystems will
464 become more vulnerable to the hot and dry climate and at increasing risk of fire events
465 (Figure 9).

466 Here we highlight the temporal changes in the distribution of carbon cycle extremes
467 and their climate drivers for the simulation *with LULCC*. East Asia experiences a large
468 number of TCEs during the 21st century (Figure 8) driven by dry climate and fire, which
469 however declines in the 22nd due to an increase in precipitation and available soil mois-

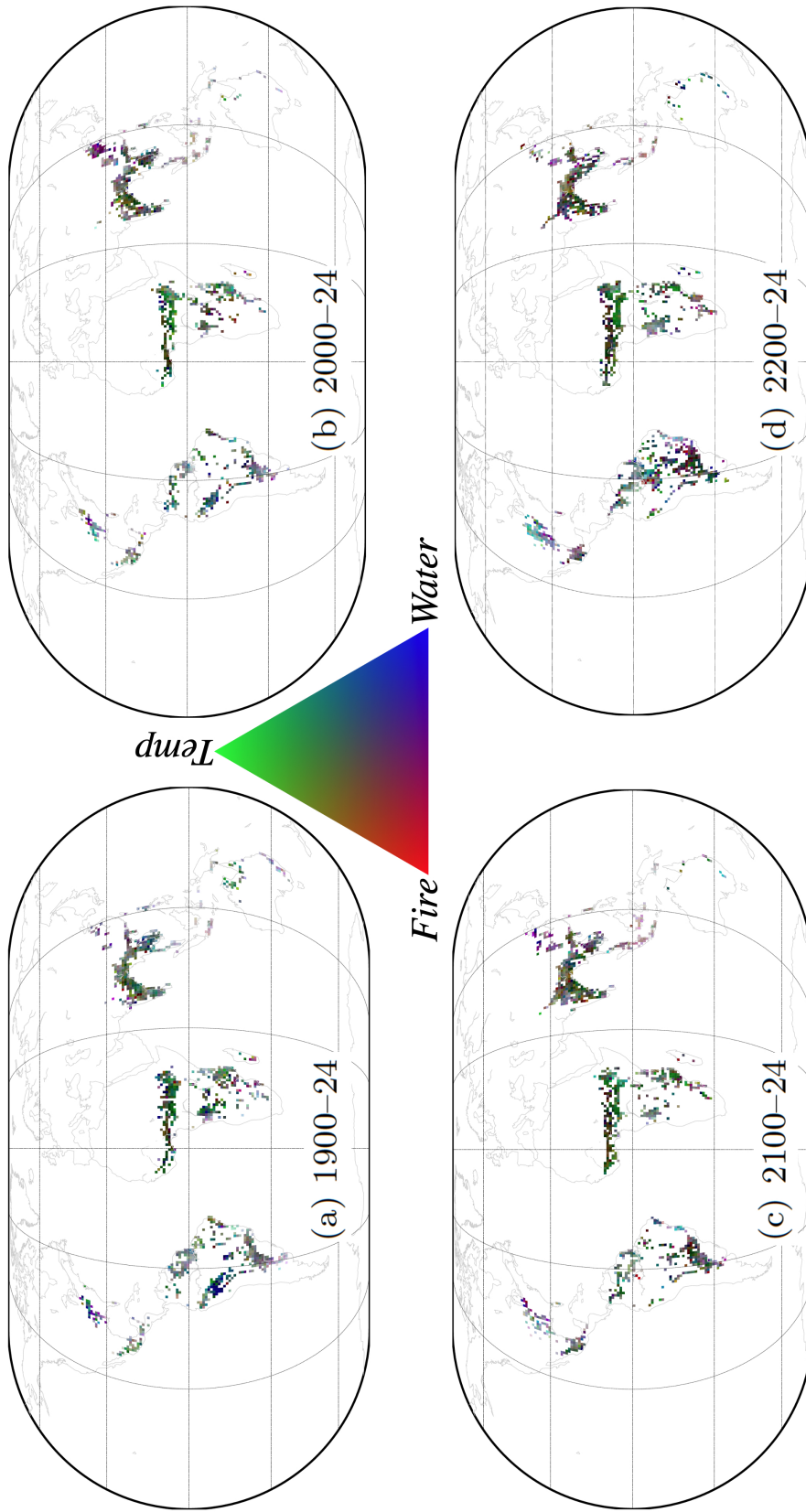


Figure 8: Spatial distribution of climate drivers causing negative TCEs in GPP for simulation with LULCC for four 25-year time windows, (a) 1900–24, (b) 2000–24, (c) 2100–24, and (d) 2200–24. The climate drivers are pooled in three colors, red, green, and blue. Red (*Fire*) is for loss of carbon due to fire, green (*Temp*) represents monthly maximum, mean, and minimum daily temperatures (T_{\max} , T_{sa} , T_{\min} respectively), Blue (*Water*) includes monthly means of soil moisture, precipitation and $P-E$ (precipitation minus evapotranspiration). The results shown here are at 1 month lag.

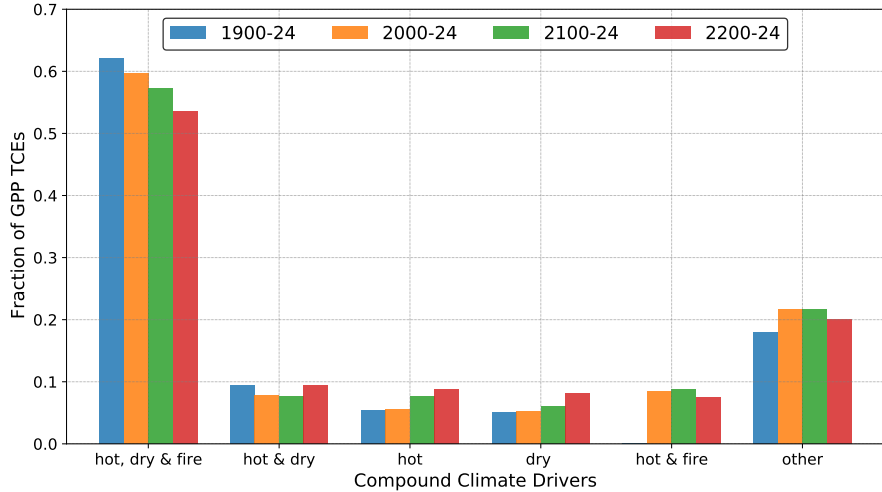


Figure 9: Attribution of temporally continuous extreme events in GPP to compound effect of climate drivers for the simulation with LULCC at lag of 1 month for 25-year time windows, (a) 1900–24, (b) 2000–24, (c) 2100–24, and (d) 2200–24. The fractions are mutually exclusive, i.e., events driven by *hot and dry* climate is not counted in either *hot* or *dry* climate driven events. Any location could be affected by one or compound climatic conditions. For example, a carbon cycle extreme could be driven by any combination of hot or cold, dry or wet, and with or without fire. We only show the combination of driving climate drivers that have total fraction of more than 0.05. The combined effect of hot and dry climate accompanied by fire leads to most negative TCE events in GPP.

ture. The Savannas near Congo in Africa display an increased vulnerability of vegetation to fire and hot temperatures. The impact of LULCC in Savannas is prominent after 2100 (Figures S5(d) and 8(d)) when the pattern of dominant drivers change from temperature-driven (green color) to a compound effect of increase in dry, hot, and fire conditions (gray color). The contiguous United States (CONUS) experiences more GPP TCEs, especially in the 23rd century (Figure 8(d)), driven by hot temperature and water limitation (highlighted in cyan color). Indonesia and its neighboring islands show increasing GPP TCEs attributed to a combination of hot temperatures and fire. The number of negative TCEs in South America are approximately the same for periods in Figures 8(a), 8(b) and 8(c) except for the period 2200–24 (Figure 8(d)) when the extremes show a large increase. During 2200–24, South America shows a drastic increase in negative TCEs that is attributed primarily to dry, hot, and fire conditions (represented by gray color). Africa experiences an increase in the number of GPP TCEs attributed to hot climate, and, in the far future (2101–2300), witnesses an increased frequency of fire events. Australia's east coast also exhibits an increase in GPP TCEs because of water limitation, dry climate, and they are accompanied by fires in the far future. The South and Southeast Asia (composed of India, Myanmar, Thailand, and Cambodia) experiences an increase in TCEs in GPP over time. These Asian regions where primary forest were converted to cropland (Hurt et al., 2011), saw an increase in fire-driven extreme events in GPP, highlighting a rising vulnerability to fire events due to LULCC.

5 Discussion

5.1 Regional Analysis of Climate Change Impact on Climate Drivers and Negative Carbon Cycle Extremes

Most climate models show an increase in the interannual variability of land-atmosphere CO₂ exchange over time (Keenan et al., 2012). The increasing atmospheric CO₂ concentration influences climate through its radiative effect (i.e., Greenhouse effect) and indirectly through physiological effect (reduced plant transpiration) (Cao et al., 2010). The increasing radiative effects cause changes in circulation, impacting precipitation, soil moisture, and global scale water cycle. Increase in precipitation and CO₂ fertilization and reduction in stomatal conductance could lead to an increase in GPP; however, droughts, heatwaves and fires curtail plant photosynthesis (Swann et al., 2016). Under climate change, while most regions experience an increase in mean GPP, some regions exhibit a decline.

502 Reduction in growth rate of expected terrestrial carbon uptake below carbon emis-
503 sions could lead to weakening of carbon sink capacity (Figure S7). Increase in total GPP
504 and IAV in GPP over time contribute to the increase in magnitude of negative carbon
505 cycle extremes, defined here as negative extremes in GPP. However, some regions expe-
506 rience weakening of negative carbon cycle extremes often due to decline in total GPP,
507 and reduction in IAV of GPP and climate drivers (Figure S8). Driven by large scale cir-
508 culation changes, increasing temperature and decreasing precipitation and soil moisture
509 in Central America (CAM) lead to forest mortality, decline in GPP and weakening of
510 negative carbon cycle extremes. The decrease in precipitation in the Northern South Amer-
511 ican Tropics (NSA) and Central Amazon Basin (CAB) and increase in precipitation in
512 the Southwest Amazon Basin (SAB) is due to plant physiologic response. Langenbrun-
513 ner et al. (2019) investigated this phenomenon in the regions of the Amazon and the An-
514 des and found that under increased atmospheric CO₂, stomatal conductance decreases,
515 reducing water loss through transpiration, which decreases the convective activity and
516 causes a reduction in rainfall over the Amazon Basin (CAB, NSA) and increases mois-
517 ture advection by low-level westward jets towards the Andes, leading to increases in the
518 rainfall over the Andes (SAB). Reducing variability and increasing precipitation over SAB
519 increase available soil moisture increasing regional GPP, however with reduced IAV, re-
520 sulting in weakening of negative carbon cycle extremes. Although CAB witnesses a de-
521 cline in precipitation it demonstrates an increase in GPP likely due to slight reduction
522 in soil moisture and large CO₂ fertilization effect which compensates for the reduction
523 in soil moisture. Hence, in CAB both GPP and IAV in GPP increases over time caus-
524 ing strengthening of negative carbon cycle extremes. These regional patterns of changes
525 in GPP, negative carbon cycle extremes, and climate drivers are seen across the globe.
526 For example, the regional changes in Northern Guinea, Southern Guinea, Central Guinea
527 and Indonesia resemble the processes in CAM, SAB, CAB and CAM, respectively. Ad-
528 ditional feedbacks due to LULCC – as tropical forests are replaced with crops or grass-
529 lands that transpire less than forests, further reducing rainfall over the Amazon – causes
530 hotter and drier climate with an increasing risk of fire and larger losses of carbon up-
531 take (Figures S9 and S10).

532 Our robust attribution analysis based on successive time windows captures the changes
533 in the anomalies of climate drivers and carbon cycle. During 1900–24 and 2000–24, most
534 of the negative TCEs in GPP that occurred in SAB (Figure 8), were due to water lim-

535 itation (highlighted by the blue color in the RGB maps). With increased water avail-
 536 ability in SAB (Langenbrunner et al., 2019), the effects of heat associated with temper-
 537 ature increases are mitigated and the number of negative carbon cycle extremes reduces.
 538 The decrease in precipitation in NSA led to a reduction in soil moisture, resulting in a
 539 hot and dry climate, thus making the vegetation prone to fire at high temperatures (the
 540 compound effect is highlighted by the gray color). The reduced GPP in NSA over time
 541 further leads to a fewer number of negative carbon cycle extremes (Figure 8). Large IAV
 542 and anomalies in GPP in CAB lead to increased concentration of negative TCEs in GPP
 543 driven possibly due to combined effect of increased hot, dry, and fire events (shown in
 544 gray color).

545 5.2 Drivers and Triggers of Carbon Cycle Extremes

546 A grid cell could experience any number of extreme events of any length during suc-
 547 cessive 25 year time windows from 1850 through 2300. Our methodology helps identify
 548 long temporally continuous extremes which represent large magnitude carbon extremes
 549 and have higher significant regression coefficient. We use this methodology to identify
 550 the prevailing climatic conditions that act as triggers for an extreme and the conditions
 551 that cause an extreme to persist. We demonstrate the findings from Chaco Province in
 552 Argentina where the major plant functional type is broadleaf deciduous tree (43%).

553 Under the simulation *without LULCC* and the time period 2000–24, the total num-
 554 ber of positive TCE events in GPP were seven with a total duration of 53 months, which
 555 were greater than the total five negative TCEs in GPP with a total duration of 40 months
 556 (Table S2). The total gain in carbon uptake was 35.17 TgC, which was greater than the
 557 total loss in carbon uptake of –28.15 TgC, resulting in a net gain in carbon during TCE
 558 events. Under the simulation *with LULCC*, during the same period of 2000–24 the to-
 559 tal number of negative GPP TCEs (6 events, 57 months) were greater than positive TCEs
 560 (5 events, 35 months). Thus, the total loss in carbon uptake (–35.86 TgC) *with LULCC*
 561 was higher than the gain in carbon uptake (23.87 TgC). While this region had a net gain
 562 in carbon uptake of 7.02 TgC for the simulation *without LULCC*, and it had a net loss
 563 in carbon uptake of –11.99 TgC for the simulation *with LULCC*. The increase in neg-
 564 ative extremes in GPP with net losses in carbon uptake demonstrates the role of human-
 565 induced LULCC in negatively affecting carbon uptake capacity.

We performed a qualitative investigation of every negative and positive TCEs in GPP (Figure S11) using normalized time series of GPP, GPP anomalies and anomalies of major climate drivers (*Prcp*, *Soilmoist*, *T_{max}*, and *Fire*). Most positive TCEs in GPP were driven by increase in precipitation, followed by rise in soil moisture and decline in *T_{max}*. Most negative extremes in GPP were driven by decline in precipitation and rising *T_{max}*, which cause high evapotranspiration and loss of soil moisture, eventually creating dry and hot conditions that cause fire events. Some of the negative extremes in these regions were also found to be driven by hot and dry events without fire.

To identify the triggers of carbon cycle extremes, we define the onset period of GPP TCEs as first-quarter of every TCE. The regression onset period of GPP TCEs and anomalies of climate drivers were computed with consideration of the lagged response of climate drivers on GPP TCEs. The lagged soil moisture anomalies were highly correlated ($p < 0.01$) with entire duration of TCE events (persistence, Table S3), and the lagged precipitation anomalies were highly correlated with the onset (trigger, Table S4) of TCE events in the Chaco Province.

For the simulation with CO₂ only forcing (i.e. *without LULCC*) during time period 2000–24, the correlation coefficient, for the whole duration of GPP TCEs, was highest for soil moisture anomalies at a lag of 1 month. The precipitation anomalies had high positive correlations with GPP TCEs (i.e., reduction in precipitation was correlated with a decrease in GPP) at lags of 3 and 4 months. *T_{max}* and *Fire* had large negative correlations with GPP anomalies (i.e., increase in temperature correlates with a decrease in GPP or increase in carbon uptake loss) at a lag of 2 months. Hence, for a negative GPP TCE event, the compound effect of a decline in precipitation followed by increase in temperature caused a reduction of soil moisture, resulting in hot and dry conditions, increasing the probability of occurrence of fire and causing a long negative TCE event (*Prcp > T_{max} > Soilmoist > TCE*). For the same region under simulation *with LULCC*, the dominant trigger was *T_{max}* (Table S5) followed by precipitation. Therefore, human-induced LULCC coupled with increasing CO₂ levels tends to enhance the vulnerability and loss in vegetation due to hot and non-dry climate conditions, resulting in more negative extremes in GPP. The analysis illustrates the strength of our methodology in identifying the evolution of carbon cycle extremes for multiple conditions and at fine resolution.

598 5.3 Limitations of CESM1(BGC)

599 The ILAMB benchmarking scores (Collier et al., 2018) of the carbon fluxes and cli-
600 mate drivers indicate that CESM1(BGC) is among the best CMIP5 models (Table S1).
601 However, the Community Land Model version 4 (CLM4), the land model used in the CESM1(BGC)
602 (Oleson et al., 2010), had some limitations which could potentially impact some of our
603 findings. The simulated GPP by CLM4 had a positive bias across the globe compared
604 to FLUXNET eddy covariance tower estimates due to lack of colimitation of GPP to canopy
605 scaling and parameterization of leaf photosynthesis kinetics (G. B. Bonan et al., 2011).
606 With improvements in the model parameterizations of radiative transfer, leaf photosyn-
607 thesis and stomatal conductance, canopy scaling of leaf processes, inclusion of multilayer
608 canopy model, and updated maximum rate of electron transfer parameters (G. B. Bo-
609 nan et al., 2011; G. B. Bonan, Oleson, et al., 2012), the positive bias in GPP was reduced.
610 With inclusion of vertically resolved CN model in CLM4.5 (Koven et al., 2013), the pos-
611 itive bias in GPP was further improved and terrestrial carbon storage increased consis-
612 tently with observations. In the current study focused on the patterns of carbon cycle
613 extremes, the positive bias of GPP was likely captured by trend and removed for cal-
614 culation of GPP anomalies. However, any associated increase in the IAV of GPP cor-
615 responding to positive bias of GPP would increase the magnitude of GPP anomalies and
616 both negative and positive GPP extremes. Thus, there is a potential to overestimate the
617 magnitude of both negative and positive GPP extremes but the relative comparison is
618 insightful and most likely not affected by this limitation of CLM4.

619 CLM4 lacks representation of dynamic crop, thus the cooling effects in irrigated
620 lands, changes in the sensible and latent heat, and soil carbon change are not well rep-
621 resented in CLM4.0 but were improved in the CLM5.0 (Lombardozzi et al., 2020). The
622 simulated climate-carbon feedbacks in CLM4 assume an instantaneous response of plant
623 physiological processes to changes in temperature (Lombardozzi et al., 2015). With in-
624 clusion of temperature acclimation, though the ecosystem carbon storage pool grew (mostly
625 in higher latitudes), the effect on photosynthesis of tropical regions was minimal. Since
626 most of the detected extremes in the tropical forest and other high biomass regions, the
627 lack of representation of agriculture and temperature acclimation on GPP are not ex-
628 pected to have significant effect on the analysis of extremes.

6 Conclusions

Using the fully-coupled Earth system model, CESM1(BGC), we analyzed the development of extreme events in GPP and attributed those carbon cycle extremes to climate drivers from the year 1850 through 2300 for simulations *with* and *without LULCC*. The changes in land cover directly modify the biogeophysical and biogeochemical feedbacks of terrestrial vegetation and indirectly through the physiological responses of vegetation on climate drivers, leading to increase in interannual variability in GPP and higher magnitude of GPP anomalies. Relative to the simulation *without LULCC*, the simulation *with LULCC* exhibited increased variability in GPP and higher intensity, duration, extent, and frequency of extremes in GPP. These characteristics were greater for negative extremes in GPP than positive extremes, implying larger than expected losses in carbon uptake than carbon gains. Although the total GPP for the simulation *with LULCC* was less than the total GPP *without LULCC*, the simulation *with LULCC* showed a sharper decline of carbon uptake of -6.9% in the near future (1850–2100) and -10% in the far future (2100–2300) with respect to total GPP *without LULCC*.

Increasing atmospheric CO₂ concentrations drive growth in vegetation photosynthesis or GPP due to carbon fertilization, and reduction in stomatal conductance. Due to circulation changes, a few regions witness a decrease in precipitation, creating a drier climate that when supplemented with warmer temperatures lead to decline in GPP, such as the regions of the eastern Amazon and Central America. Reducing magnitudes of GPP over time and analogous decreases in the interannual variability of GPP produce weakening of negative carbon cycle or GPP extremes in the Amazon. Moreover, the weakening of other negative carbon cycle extremes could be a result of less variable and benign climatic conditions for vegetation productivity, as seen around the Andes. Hence, it is imperative to inspect trends in GPP and negative carbon cycle extremes simultaneously to understand the nature of changes in extremes and their implications at regional scales.

We found that the duration of GPP TCEs increased with higher CO₂ concentration. The duration and impact of negative TCEs in GPP are enhanced when human-induced LULCC was considered, resulting in increased loss in carbon uptake. We illustrated this with the case study of the Chaco Province in Argentina that had a net gain in carbon

660 uptake (7.02 TgC) during 2000–24 in the simulation *without LULCC* and while a net
661 loss in carbon uptake (−11.99 TgC) in the simulation *with LULCC*.

662 The dominant climate driver was soil moisture that had highest correlations with
663 GPP extremes ($p < 0.05$) and the correlations were mostly positive, indicating that anomalous
664 decrease in soil moisture or drier climate conditions cause anomalous reductions in
665 GPP. Other major individual drivers were hot temperatures and fire. Fire was a dominant
666 climate driver, especially after 2100 in the simulation *with LULCC*, highlighting
667 the increased vulnerability of ecosystems to fire events due to the impact of human activities
668 on ecosystems. We also found that the decline in precipitation triggers a negative
669 carbon cycle TCE event, but the reduction in soil moisture or water limitation was
670 the dominant driver for those negative carbon cycle TCE events to persist. The compound
671 effects of climate drivers were also analyzed, and an increasing number of regions
672 under carbon cycle extremes were attributed to hot and dry conditions. The largest fraction
673 of negative carbon cycle extremes were driven by the compound effects of hot, dry,
674 and fire events. Warmer conditions under climate change increases the risk of occurrence
675 of fire events and their impacts on the carbon cycle and extremes of the future.

676 This study presents a detailed analysis of detection and identification of carbon cycle
677 extreme events, how these extremes evolve from 1850 through 2300, and how human-
678 induced LULCC alters them using a fully coupled Earth system model forced with the
679 RCP 8.5 and ECP 8.5 CO₂ concentration scenarios. It also attributes the climate drivers
680 of such extremes in carbon cycle, and analyzes the changing patterns and dominance of
681 climate drivers, under *with* and *without LULCC* scenarios. Study provides new insights
682 into the contribution of human activities in altering carbon cycle extremes and the
683 vulnerability of terrestrial vegetation and associated ecosystem services that could present
684 increasing risks to human lives, wildlife, and food security.

Acknowledgments

We thank the Community Earth System Model (CESM) Biogeochemistry Working Group (BGCWG) for performing the CESM1(BGC) simulations analyzed in this study. This research was supported by the Reducing Uncertainties in Biogeochemical Interactions through Synthesis and Computation (RUBISCO) Science Focus Area, which is sponsored by the Regional and Global Model Analysis (RGMA) activity of the Earth & Environmental Systems Modeling (EESM) Program in the Earth and Environmental Systems Sciences Division (EESSD) of the Office of Biological and Environmental Research (BER) in the US Department of Energy Office of Science. This research used resources of the Compute and Data Environment for Science (CADES) at the Oak Ridge National Laboratory, which is managed by UT-Battelle, LLC, for the US Department of Energy under Contract No. DE-AC05-00OR22725.

Open Research**Data Availability Statement**

The CESM1(BGC) model output used for detection and attribution of carbon cycle extremes in the study are available at <https://doi.org/10.5281/zenodo.5548153>. Data analysis was performed in Python, and all analysis codes are publicly available on GitHub at https://github.com/sharma-bharat/Codes_Carbon_Extremes_2300 and archived at <https://doi.org/10.5281/zenodo.6147120>.

704 References

- Baldwin, J. W., Derry, J. B., Vecchi, G. A., & Oppenheimer, M. (2019). Temporally compound heat wave events and global warming: An emerging hazard. *Earth's Future*, 7(4), 411–427. doi: 10.1029/2018EF000989
- Ban, N., Schmidli, J., & Schär, C. (2015). Heavy precipitation in a changing climate: Does short-term summer precipitation increase faster? *Geophysical Research Letters*, 42(4), 1165–1172. doi: 10.1002/2014GL062588
- Bonan, G. (2015). *Ecological climatology: Concepts and applications* (3rd ed.). Cambridge University Press. doi: 10.1017/CBO9781107339200
- Bonan, G. B., DeFries, R. S., Coe, M. T., & Ojima, D. S. (2012). Land use and climate. In *Land change science. remote sensing and digital image processing* (Vol. 6, pp. 301–314). Springer. doi: 10.1007/978-1-4020-2562-4_17
- Bonan, G. B., Lawrence, P. J., Oleson, K. W., Levis, S., Jung, M., Reichstein, M., ... Swenson, S. C. (2011). Improving canopy processes in the community land model version 4 (clm4) using global flux fields empirically inferred from fluxnet data. *Journal of Geophysical Research: Biogeosciences*, 116(G2). doi: 10.1029/2010JG001593
- Bonan, G. B., Oleson, K. W., Fisher, R. A., Lasslop, G., & Reichstein, M. (2012). Reconciling leaf physiological traits and canopy flux data: Use of the try and fluxnet databases in the community land model version 4. *Journal of Geophysical Research: Biogeosciences*, 117(G2). doi: 10.1029/2011JG001913
- Cao, L., Bala, G., Caldeira, K., Nemani, R., & Ban-Weiss, G. (2010). Importance of carbon dioxide physiological forcing to future climate change. *Proceedings of the National Academy of Sciences*, 107(21), 9513–9518. doi: 10.1073/pnas.0913000107
- Chylek, P., Tans, P., Christy, J., & Dubey, M. K. (2018, Jan). The carbon cycle response to two el nino types: an observational study. *Environmental Research Letters*, 13(2), 024001. doi: 10.1088/1748-9326/aa9c5b
- Collier, N., Hoffman, F. M., Lawrence, D. M., Keppel-Aleks, G., Koven, C. D., Riley, W. J., ... Randerson, J. T. (2018). The international land model benchmarking (ilamb) system: Design, theory, and implementation. *Journal of Advances in Modeling Earth Systems*, 10(11), 2731–2754. doi: 10.1029/2018MS001354
- Flach, M., Brenning, A., Gans, F., Reichstein, M., Sippel, S., & Mahecha, M. D.

- (2020). Vegetation modulates the impact of climate extremes on gross primary production. *Biogeosciences Discussions*, 2020, 1–20. doi: 10.5194/bg-2020-80
- Frank, D., Reichstein, M., Bahn, M., Thonicke, K., Frank, D., Mahecha, M. D., ... Zscheischler, J. (2015). Effects of climate extremes on the terrestrial carbon cycle: concepts, processes and potential future impacts. *Global Change Biology*, 21(8), 2861–2880. doi: 10.1111/gcb.12916
- Golyandina, N., Nekrutkin, V., & Zhigljavsky, A. A. (2001). *Analysis of time series structure: Ssa and related techniques* (1st ed.). Chapman and Hall/CRC. doi: 10.1201/9781420035841
- Hoffman, F. M., Randerson, J. T., Arora, V. K., Bao, Q., Cadule, P., Ji, D., ... Wu, T. (2014). Causes and implications of persistent atmospheric carbon dioxide biases in earth system models. *Journal of Geophysical Research: Biogeosciences*, 119(2), 141–162. doi: 10.1002/2013JG002381
- Hubau, W., Lewis, S. L., Phillips, O. L., Affum-Baffoe, K., Beeckman, H., Cuní-Sánchez, A., ... others (2020). Asynchronous carbon sink saturation in African and Amazonian tropical forests. *Nature*, 579(7797), 80–87. doi: 10.1038/s41586-020-2035-0
- Hurttt, G. C., Chini, L. P., Frolking, S., Betts, R. A., Feddema, J., Fischer, G., ... Wang, Y. P. (2011, Aug 09). Harmonization of land-use scenarios for the period 1500–2100: 600years of global gridded annual land-use transitions, wood harvest, and resulting secondary lands. *Climatic Change*, 109(1), 117. doi: 10.1007/s10584-011-0153-2
- Ichii, K., Hashimoto, H., Nemani, R., & White, M. (2005). Modeling the inter-annual variability and trends in gross and net primary productivity of tropical forests from 1982 to 1999. *Global and Planetary Change*, 48(4), 274–286. doi: 10.1016/j.gloplacha.2005.02.005
- Keenan, T., Baker, I., Barr, A., Ciais, P., Davis, K., Dietze, M., ... Richardson, A. D. (2012). Terrestrial biosphere model performance for inter-annual variability of land-atmosphere CO₂ exchange. *Global Change Biology*, 18(6), 1971–1987. doi: 10.1111/j.1365-2486.2012.02678.x
- Koven, C. D., Riley, W. J., Subin, Z. M., Tang, J. Y., Torn, M. S., Collins, W. D., ... Swenson, S. C. (2013). The effect of vertically resolved soil biogeochemistry and alternate soil c and n models on c dynamics of clm4. *Biogeosciences*, 10(11),

- 770 7109–7131. doi: 10.5194/bg-10-7109-2013
- 771 Lamarque, J.-F., Bond, T. C., Eyring, V., Granier, C., Heil, A., Klimont, Z., ...
- 772 van Vuuren, D. P. (2010). Historical (18502000) gridded anthropogenic and
- 773 biomass burning emissions of reactive gases and aerosols: methodology and
- 774 application. *Atmospheric Chemistry and Physics*, 10(15), 7017–7039. doi:
- 775 10.5194/acp-10-7017-2010
- 776 Langenbrunner, B., Pritchard, M. S., Kooperman, G. J., & Randerson, J. T. (2019).
- 777 Why does Amazon precipitation decrease when tropical forests respond to increasing CO₂? *Earth's Future*, 7(4), 450–468. doi: 10.1029/2018EF001026
- 778 Lawrence, D. M., Hurtt, G. C., Arneth, A., Brovkin, V., Calvin, K. V., Jones, A. D.,
- 779 ... Shevliakova, E. (2016). The Land Use Model Intercomparison Project (LU-
- 780 MIP) contribution to CMIP6: Rationale and experimental design. *Geoscientific*
- 781 *Model Development*, 9(9), 2973–2998. doi: 10.5194/gmd-9-2973-2016
- 782 Lawrence, P. J., Feddema, J. J., Bonan, G. B., Meehl, G. A., O'Neill, B. C., Ole-
- 783 son, K. W., ... Thornton, P. E. (2012). Simulating the biogeochemical and
- 784 biogeophysical impacts of transient land cover change and wood harvest in the
- 785 community climate system model (ccsm4) from 1850 to 2100. *Journal of Climate*,
- 786 25(9), 3071–3095. doi: 10.1175/JCLI-D-11-00256.1
- 787 Le Quéré, C., Andrew, R. M., Friedlingstein, P., Sitch, S., Hauck, J., Pongratz, J.,
- 788 ... Zheng, B. (2018). Global carbon budget 2018. *Earth System Science Data*,
- 789 10(4), 2141–2194. doi: 10.5194/essd-10-2141-2018
- 790 Lindsay, K., Bonan, G. B., Doney, S. C., Hoffman, F. M., Lawrence, D. M., Long,
- 791 M. C., ... Thornton, P. E. (2014). Preindustrial-control and twentieth-century
- 792 carbon cycle experiments with the earth system model cesm1(bgc). *Journal of*
- 793 *Climate*, 27(24), 8981–9005. doi: 10.1175/JCLI-D-12-00565.1
- 794 Lombardozzi, D. L., Bonan, G. B., Smith, N. G., Dukes, J. S., & Fisher, R. A.
- 795 (2015). Temperature acclimation of photosynthesis and respiration: A key uncer-
- 796 tainty in the carbon cycle-climate feedback. *Geophysical Research Letters*, 42(20),
- 797 8624–8631. doi: 10.1002/2015GL065934
- 798 Lombardozzi, D. L., Lu, Y., Lawrence, P. J., Lawrence, D. M., Swenson, S., Oleson,
- 799 K. W., ... Ainsworth, E. A. (2020). Simulating agriculture in the community
- 800 land model version 5. *Journal of Geophysical Research: Biogeosciences*, 125(8),
- 801 e2019JG005529. doi: 10.1029/2019JG005529

- 803 Mahowald, N. M., Randerson, J. T., Lindsay, K., Munoz, E., Doney, S. C.,
804 Lawrence, P., ... Hoffman, F. M. (2017). Interactions between land use change
805 and carbon cycle feedbacks. *Global Biogeochemical Cycles*, 31(1), 96–113. doi:
806 10.1002/2016GB005374
- 807 Marcolla, B., Migliavacca, M., Rödenbeck, C., & Cescatti, A. (2020). Patterns and
808 trends of the dominant environmental controls of net biome productivity. *Biogeosciences*,
809 17(8), 2365–2379. doi: 10.5194/bg-17-2365-2020
- 810 Moore, J. K., Fu, W., Primeau, F., Britten, G. L., Lindsay, K., Long, M., ... Ran-
811 derson, J. T. (2018). Sustained climate warming drives declining marine biological
812 productivity. *Science*, 359(6380), 1139–1143. doi: 10.1126/science.aa06379
- 813 O’Gorman, P. A. (2015, Jun 01). Precipitation extremes under climate change. *Cur-
814 rent Climate Change Reports*, 1(2), 49–59. doi: 10.1007/s40641-015-0009-3
- 815 Oleson, K. W., Lawrence, D. M., Bonan, G. B., Flanner, M. G., Kluzek, E.,
816 Lawrence, P. J., ... Zeng, X. (2010, March 1). *Technical description of version
817 4.0 of the Community Land Model (CLM)* (Technical Note Nos. NCAR/TN-
818 478+STR). Boulder, Colorado, USA: National Center for Atmospheric Re-
819 search. Retrieved from http://www.cesm.ucar.edu/models/cesm1.0/clm/CLM4_Tech_Note.pdf
- 820 Pan, S., Yang, J., Tian, H., Shi, H., Chang, J., Ciais, P., ... Zhao, F. (2019). Cli-
821 mate extreme versus carbon extreme: Responses of terrestrial carbon fluxes to
822 temperature and precipitation. *Journal of Geophysical Research: Biogeosciences*,
823 125(4), e2019JG005252. doi: 10.1029/2019JG005252
- 824 Piao, S., Wang, X., Wang, K., Li, X., Bastos, A., Canadell, J. G., ... Sitch, S.
825 (2020). Interannual variation of terrestrial carbon cycle: Issues and perspectives.
826 *Global Change Biology*, 26(1), 300–318. doi: 10.1111/gcb.14884
- 827 Pitman, A. J., de Noblet-Ducoudré, N., Avila, F. B., Alexander, L. V., Boisier, J.-P.,
828 Brovkin, V., ... Volodire, A. (2012). Effects of land cover change on tempera-
829 ture and rainfall extremes in multi-model ensemble simulations. *Earth System
830 Dynamics*, 3(2), 213–231. doi: 10.5194/esd-3-213-2012
- 831 Poveda, G., Jaramillo, A., Gil, M. M., Quiceno, N., & Mantilla, R. I. (2001). Sea-
832 sonally in enso-related precipitation, river discharges, soil moisture, and vege-
833 tation index in colombia. *Water Resources Research*, 37(8), 2169–2178. doi:
834 10.1029/2000WR900395

- 836 Reichstein, M., Bahn, M., Ciais, P., Frank, D., Mahecha, M. D., Seneviratne, S. I.,
 837 ... Wattenbach, M. (2013). Climate extremes and the carbon cycle. *Nature*,
 838 500(7462), 287–295. doi: 10.1038/nature12350
- 839 Seneviratne, S. I., & Hauser, M. (2020). Regional climate sensitivity of climate ex-
 840 tremes in cmip6 vs cmip5 multi-model ensembles. *Earth's Future*, e2019EF001474.
 841 doi: 10.1029/2019EF001474
- 842 Seneviratne, S. I., Nicholls, N., Easterling, D., Goodess, C. M., Kanae, S., Kossin,
 843 J., ... Zhang, X. (2012). Changes in climate extremes and their impacts on the
 844 natural physical environment. In *Managing the risks of extreme events and disas-
 845ters to advance climate change adaptation* (pp. 109–230). Cambridge Univ. Press,
 846 Cambridge, U.K., and New York. ([Field, C.B., V. Barros, T.F. Stocker, D. Qin,
 847 D.J. Dokken, K.L. Ebi, M.D. Mastrandrea, K.J. Mach, G.-K. Plattner, S.K. Allen,
 848 M. Tignor, and P.M. Midgley (eds.)]. A Special Report of Working Groups I and
 849 II of the Intergovernmental Panel on Climate Change (IPCC))
- 850 Swann, A. L. S., Hoffman, F. M., Koven, C. D., & Randerson, J. T. (2016). Plant
 851 responses to increasing CO_2 reduce estimates of climate impacts on
 852 drought severity. *Proceedings of the National Academy of Sciences*, 113(36),
 853 10019–10024. Retrieved from <https://www.pnas.org/doi/abs/10.1073/pnas.1604581113> doi: 10.1073/pnas.1604581113
- 855 Williams, I. N., Torn, M. S., Riley, W. J., & Wehner, M. F. (2014, Sep). Impacts of
 856 climate extremes on gross primary production under global warming. *Environmen-
 857tal Research Letters*, 9(9), 094011. doi: 10.1088/1748-9326/9/9/094011
- 858 Wu, Z., K. Schneider, E., Kirtman, B., Sarachik, E., Huang, N., & J. Tucker,
 859 C. (2008, 12). The modulated annual cycle: An alternative reference frame
 860 for climate anomalies. *Climate Dynamics*, 31, 823–841. doi: 10.1007/s00382-008-0437-z
- 862 Xian, G. Z., Loveland, T., Munson, S. M., Vogelmann, J. E., Zeng, X., & Homer,
 863 C. J. (2020, September). Climate sensitivity to decadal land cover and land use
 864 change across the conterminous United States. *Global and Planetary Change*, 192,
 865 103262. doi: 10.1016/j.gloplacha.2020.103262
- 866 Xu, M., Mahajan, S., Hoffman, F. M., & Shi, X. (2019, November 8). Evalu-
 867 ating carbon extremes in a coupled climate-carbon cycle simulation. In *Pro-
 868 ceedings of the 2019 IEEE international conference on data mining workshops*

- 869 (ICDMW 2019) (pp. 303–310). Conference Publishing Services (CPS). doi:
870 10.1109/ICDMW.2019.00052
- 871 Zhang, T., Xu, M., Xi, Y., Zhu, J., Tian, L., Zhang, X., ... Zhang, Y. (2014, 12).
872 Lagged climatic effects on carbon fluxes over three grassland ecosystems in China.
873 *Journal of Plant Ecology*, 8(3), 291–302. doi: 10.1093/jpe/rtu026
- 874 Zhu, Z., Piao, S., Myneni, R., Huang, M., Zeng, Z., Canadell, J., ... Zeng, N. (2016,
875 04). Greening of the earth and its drivers. *Nature Climate Change*, 6. doi: 10
876 .1038/nclimate3004
- 877 Zscheischler, J., Reichstein, M., von Buttlar, J., Mu, M., Randerson, J. T., & Ma-
878 hecha, M. D. (2014). Carbon cycle extremes during the 21st century in cmip5
879 models: Future evolution and attribution to climatic drivers. *Geophysical Research
Letters*, 41(24), 8853–8861. doi: 10.1002/2014GL062409
- 880 Zscheischler, J., Westra, S., Van Den Hurk, B. J., Seneviratne, S. I., Ward, P. J.,
881 Pitman, A., ... Zhang, X. (2018). Future climate risk from compound events.
882 *Nature Climate Change*, 8(6), 469–477. doi: 10.1038/s41558-018-0156-3

